



Simplified mitral valve modeling for prospective clinical application of left ventricular fluid dynamics

Dario Collia^a, Marija Vukicevic^b, Valentina Meschini^c, Luigino Zovatto^a, Gianni Pedrizzetti^{a,*}

^a Department of Engineering and Architecture, University of Trieste, Trieste, Italy

^b Department of Cardiology, Methodist DeBakey Heart & Vascular Center, Houston Methodist Hospital, Houston, TX, USA

^c Gran Sasso Science Institute, L'Aquila, Italy



ARTICLE INFO

Article history:

Received 4 February 2019

Received in revised form 5 August 2019

Accepted 13 August 2019

Available online 20 August 2019

Keywords:

Biofluid dynamics

Cardiovascular flow

Immersed boundary methods

Computational fluid dynamics

Fluid-structure interaction

ABSTRACT

The fluid dynamics inside the left ventricle of the human heart is considered a potential indicator of long term cardiovascular outcome. In this respect, numerical simulations can play an important role for integrating existing technology to reproduce flow details and even conditions associated to virtual therapeutic solutions. Nevertheless, numerical models encounter serious practical difficulties in describing the interaction between flow and surrounding tissues due to the limited information inherently available in real clinical applications.

This study presents a computational method for the fluid dynamics inside the left ventricle designed to be efficiently integrated in clinical scenarios. It includes an original model of the mitral valve dynamics, which describes an asymptotic behavior for tissues with no elastic stiffness other than the constrain of the geometry obtained from medical imaging; in particular, the model provides an asymptotic description without requiring details of tissue properties that may not be measurable *in vivo*.

The advantages of this model with respect to a valveless orifice and its limitations with respect to a complete tissue modeling are verified. Its performances are then analyzed in details to ensure a correct interpretation of results. It represents a potential option when information about tissue mechanical properties is insufficient for the implementations of a full fluid-structure interaction approach.

© 2019 Elsevier Inc. All rights reserved.

1. Introduction

Fluid dynamics is gaining increasing attention in cardiology for the influence it may have on the long-term outcome of several cardiac dysfunctions [25,29]. Numerous studies in literature reported how stresses due to the interaction between flow and tissue play a primary role in the development of embryonic hearts [1,6,14], and flow-mediated forces participate in the progression or regression of cardiac pathologies in adult hearts [11,30]. Given its potential importance, it is foreseeable that measurements of intra-cardiac fluid dynamics will soon become an integral part of the clinical evaluation process.

Recent advances in cardiovascular imaging permit, to some extent, measurement of cardiac fluid dynamics *in vivo* [24,36]; especially in the left ventricle (LV), which represents the most energetic and clinically relevant cardiac chamber.

* Corresponding author.

E-mail address: giannip@dia.units.it (G. Pedrizzetti).

However, the imaging technologies able to quantify blood flow, like Magnetic Resonance Imaging (MRI) and Echocardiography, present limitations in this respect and applications to clinical practice are still limited. Direct numerical simulation (DNS) of intraventricular fluid dynamics represents another possible approach to analyze cardiac flow in individual patients. DNS can be performed in LV geometries extracted from clinical images, as Computed Tomography (CT), MRI or Echocardiography, to reproduce the flow under realistic conditions.

Recent advances in DNS of cardiac fluid dynamics were mostly based on the immersed boundary method (IBM). That method was originally introduced from the 1970s [31,33,32], and underwent numerous developments and improvements since then [8,22,38]. In the IBM, the flow equations are resolved in a regular Cartesian grid with a distribution of fictitious forces concentrated at the immersed solid boundaries whose intensity is matched to ensure fulfillment of the boundary conditions. IBM is particularly well suited for integration with medical imaging because the extracted moving geometries are simply immersed inside the fluid domain without the need for specific mesh-generation procedures. It also allows a relatively straightforward management of closure and opening of the valves avoiding problems associated with extreme grid deformation or collapse. Recent reviews outlined the reliability of computational approaches to analyze LV fluid dynamics [23,28].

An open challenge in LV flow simulations is represented by modeling the dynamics of the mitral valve (MV) that separates the left atrium from the LV and whose dynamics influences the flow inside the LV. The MV is a bi-leaflet valve with a longer leaflet on the anterior side (on the aortic side, separating inflow and outflow tracts) and a shorter one next to the posterior LV wall. The opening and closure motion of the asymmetric MV leaflets is mainly driven by the flow with a minimal elastic resistance from the loose tissue (under normal conditions) other than the support of chordae tendineae that avoid backward displacement of the leaflets and ensure unidirectional flow. At the same time, the dynamics of the MV leaflets influences vortex formation and the flow that develops inside the LV during filling (diastole), which indirectly affects several measures that are used for medical diagnosis. In general, the knowledge of the relationship between MV dynamics and LV flow is very limited because the motion of the valvular leaflets is relatively rapid and the time resolution of current medical imaging technology does not allow a direct evaluation during examinations.

The complexity and lack of reliable in vivo measurement also make simulations of MV dynamics difficult; indeed, most numerical studies of LV fluid dynamics are performed using orifice-like valves, with a fully-open/fully-closed behavior, and did not include the dynamics of valvular leaflets. Other models of MV dynamics, after the pioneering numerical studies in the 80's [33,32], avoided dealing with the complexity of a real general fluid-structure interaction (FSI) and considered a prescribed motion for the leaflets with the main objective of verifying the differences with valveless orifices [2,37]. Realistic FSI model are challenging and are becoming progressively feasible since recently; here valve motion obeys the equation for the finite deformation of the elastic material under the action of a distribution of flow-driven pressure difference between the two sides of the leaflets [13,21,15,16,12,40,3]. Such a rigorous approach is best suited for prosthetic valves whose mechanical properties are known in details; differently, its application in a clinical context may fall short of the knowledge of the (visco-)elastic properties for the valvular tissues that are not easily quantifiable in vivo. Indeed, the mitral leaflets present an inhomogeneous structure, with variable thickness made of a non-isotropic fibrous texture near the annulus that becomes looser and thinner closer to the trailing edge [34,5,17].

In subject-specific clinical applications, elastic properties are not directly measurable and imaging tools allow extracting the geometry of the mitral valve with moderate accuracy and limited to few instances (typically fully-closed and fully-open configurations, that last some longer). This limited availability of information is commonly overcome by using average geometric models and parameters that are representative of a population, an approach that can be appropriate when investigating properties common to pathological classes. On the other hand, in individual clinical applications and in the presence of subject-specific pathological conditions, it is necessary to develop relatively simple models that can best integrate the few available data for providing information that can be included in the clinical process.

An asymptotic model for MV dynamics was previously introduced to reproduce the flow-driven motion of valvular leaflets in absence of elastic resistance [9]. That model was intrinsically limited to a dynamics described by one-degree-of-freedom only and was evaluated in an idealized valvular geometry. The present study, inspired from that model, introduces an original mathematical framework that permits to analyze the MV dynamics described by an arbitrary number of degrees of freedom. This approach may find application, in principle, to other fields where the motion of structural elements is driven by fluid flows in the asymptotic limit of negligible elastic or inertial effects. The internal forces are replaced by an intrinsic stiffness associated with the description in terms of a limited number of degrees of freedom. In the present application, this approach is integrated with imaging technology for the numerical solution of MV leaflets motion with geometry effectively obtained from individual recordings. The computational model is then subjected to an extensive verification to get confidence of its capabilities and of its limitations.

2. Computational model

2.1. Geometric descriptions

The LV is a closed cavity bounded by the lateral LV wall and by the basal surface that contains the mitral and aortic orifices representing the flow inlet and outlet, respectively. The geometry of the lateral LV wall can be obtained from several imaging technologies like CT, MRI or Echocardiography. Different modalities differ for the time and spatial resolution,

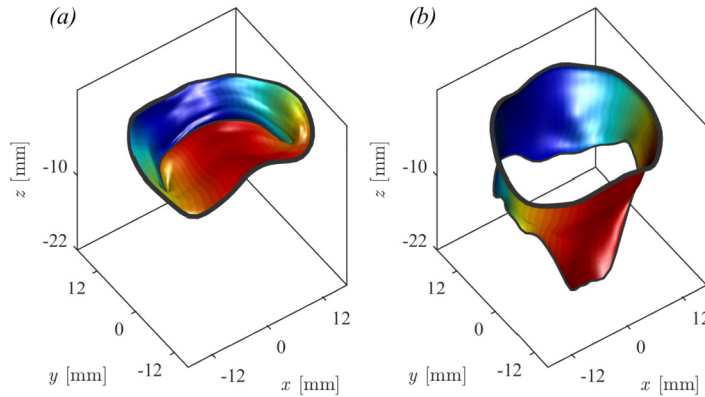


Fig. 1. Normal mitral valve surface: (a) closed systolic configuration, (b) fully open diastolic configuration; the color (red=anterior leaflet, blue=posterior leaflet) indicates the local influence of individual opening angles in a model with two degrees of freedom. (For interpretation of the colors in the figure(s), the reader is referred to the web version of this article.)

for providing multi-slice or full 3D acquisitions, and for the availability in the clinical environment. Different software solutions are usually available in the different modalities that help to identify the LV internal surface by user-assisted interactive procedures. Whatever the technology, the typical results is a dynamic cast of the moving LV cavity that we eventually described by the positions vector $\mathbf{X}(\vartheta, s, t)$, where the structured parametric coordinates, (ϑ, s) , run along the circumference and from base to apex, respectively, t is time. The usage of structured coordinates here was preferred for easier manipulation; however, unstructured (e.g. triangular) descriptions could be equally used. The position vector marks LV material points and their velocity is obtained by time differentiation.

The MV geometry can also be extracted from the same imaging technologies relying on dedicated software tools for valvular delineation. Commonly, the time resolution does not allow to reliably visualize and extract the MV geometry other than in the fully-open (peak diastole) and fully-closed (during early systole) configurations. The geometry of a normal MV, in closed and open configurations, is shown in Fig. 1 as extracted from CT [39]. Whatever the imaging technology adopted, the 3D mesh of the leaflets' surface in the two configurations was reorganized in terms of an analogous set of structured parametric coordinates, (ϑ, s) , along the circumference and extending from the annulus to the trailing edge. Additional reference measurement must then be obtained for placing the extracted MV geometry in the proper position relative to LV. This step is simplified when both LV and MV geometries are extracted from the same image set such that they are described with a common system of coordinates ensuring their automatic relative positioning. The most feasible imaging solution to this aim is given by Trans-Esophageal 3D Echocardiography (3D TEE), that is commonly used for visualization of valvular diseases, although image quality is not always optimal. However, imaging technology is rapidly evolving and segmentation options -that are out of the scope of this work- are continuously growing and improving the feasibility of reliable geometric reconstructions.

When the valve shape is recorded at two instants corresponding to the closed and the open configurations, say at $\varphi = 0$ and $\varphi = \pi/2$, respectively, where φ is the generic degree of local opening, the valve geometry at intermediate positions must be reconstructed. This is performed here as follows, at an intermediate degree of opening, φ , the position of the annulus ($s = 0$) is evaluated by linear interpolation between the closed and open configurations; then, starting from the annulus, the local metrics and the local normal is estimated from linear interpolation and integrated along the radial direction s . This simple approach can be improved when the valve geometry or other information is available at additional intermediate stages.

The MV geometry is eventually described as $\mathbf{X}_v(\vartheta, s, \varphi)$, where φ is a time-varying function that corresponds to the degree of opening. It is important to remark that at this stage there is not limitation on the number of degrees of freedom allowed for valvular movement because, theoretically, the degree of opening can be a function $\varphi(\vartheta, s, t)$. In the application presented in §4, we first described the valve with one degree of freedom assuming $\varphi(t)$ to be a constant over the valvular surface, then we considered the two leaflets moving independently with two degrees of freedom by modulating the function as

$$\varphi(\vartheta, s, t) = \varphi_2(t) + (\varphi_1(t) - \varphi_2(t)) \frac{(1 + \cos \vartheta)}{2}, \quad (1)$$

where $\varphi_1(t)$ is the opening angle of the long (anterior) leaflet and $\varphi_2(t)$ the short (posterior) leaflet. The function (1) is displayed in Fig. 1 to show the relative influence of the two leaflets in the valvular geometry.

The aortic valve at the outlet is modeled by a simple open/close behavior with no leaflets. The annulus of the MV and that of the aortic valve are then connected to the annulus of the LV valve by an automatic linear connection procedure to close the basal surface of the LV around the valves. The overall geometry of the normal LV is shown in Fig. 2.

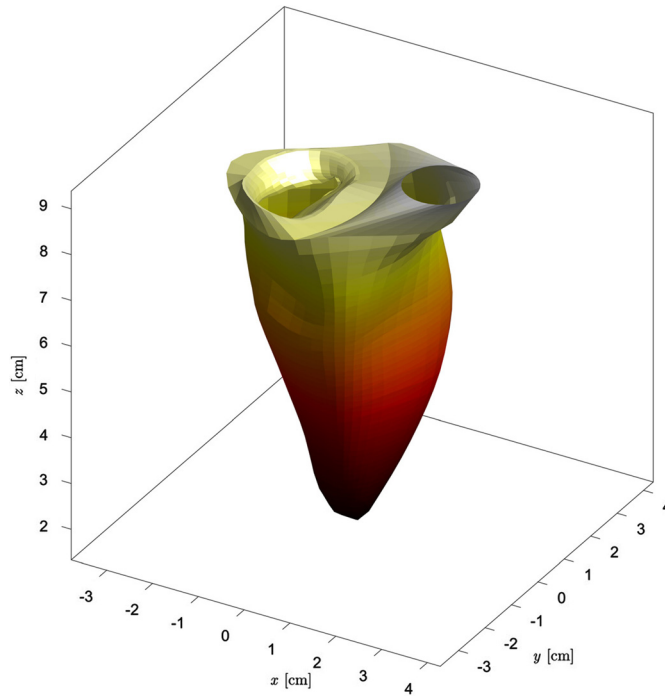


Fig. 2. Complete geometry of ventricle, mitral valve (with open leaflets) and basal surface including the open aortic orifice. Color is modulated with the vertical coordinate.

2.2. Fluid dynamics

The fluid dynamics is evaluated by numerical solution of the Navier-Stokes and continuity equations

$$\frac{\partial \mathbf{v}}{\partial t} + \mathbf{v} \cdot \nabla \mathbf{v} = -\nabla p + \nu \nabla^2 \mathbf{v}, \quad (2)$$

$$\nabla \cdot \mathbf{v} = 0; \quad (3)$$

where $\mathbf{v}(t, \mathbf{x})$ is the velocity vector field, $p(t, \mathbf{x})$ is the kinematic pressure field and ν is the kinematic viscosity (assumed $0.04 \text{ cm}^2/\text{s}$). Blood is intentionally assumed as a Newtonian fluid. Indeed, blood is a mixture of elastic corpuscular elements in an aqueous solution and either Newtonian or non-Newtonian models are approximate. However, the influence of corpuscular or non-Newtonian behavior is very small in the heart chambers [21] and it is negligible when compared with the limited accuracy of the clinical data used as input.

The numerical solution is based on an immersed boundary method previously used in numerous studies [10,9,19,20], which is briefly recalled here. Equations are solved numerically in a rectangular domain using a staggered, face-centered regular Cartesian grid where spatial derivatives are approximated by second-order centered finite differences. Time advancement is achieved using a fractional step method as follows. Velocity is preliminarily advanced in time by the Navier-Stokes equation (2) using a low-storage, third-order Runge-Kutta explicit scheme. This preliminary velocity, say $\hat{\mathbf{v}}$, that does not satisfy the incompressibility constraint (3), is corrected by adding a potential field $\delta \mathbf{v} = \nabla q$, such that $\mathbf{v} = \hat{\mathbf{v}} + \delta \mathbf{v}$ satisfies the continuity and the boundary conditions. The correction potential is found by solution of the Poisson equation

$$\nabla^2 q = -\nabla \cdot \hat{\mathbf{v}}; \quad (4)$$

and pressure is updated with q accordingly. Boundary conditions at the edge of the computational box are set periodic in the x and y directions, while they are zero pressure and normal velocity on the upper and lower ends along z , respectively. The 2D Fourier decomposition permits fast solution of the Poisson equation (4) as a sequence of tridiagonal systems for each harmonic.

Boundary conditions are also set on the moving immersed boundaries. These comprise the LV lateral wall, the basal wall and the MV leaflets, as defined above in §2.1. In addition, two cylindrical regions are added extending from a region around the mitral valve (bounded by the LV edge on the mitral side and the curve separating MV and aortic valve) and from around the aortic valve to the upper edge of the computational domain; these additional boundaries represent surrogates of atrium and aorta. They are included for numerical convenience to avoid interference between the outflow and the inflow outside the LV and to avoid nonphysical sharp corners at the edge of the LV basal plane; the potential influence of these on the

intraventricular flow is evaluated in §3.1 dedicated to numerical verifications. Following the IBM approach, the boundary conditions are imposed on the intermediate velocity $\hat{\mathbf{v}}$ at the end of the Runge-Kutta time advancement before imposing the correction obtained by (4) [8].

Given that the immersed boundaries do not coincide with the computational grid, a local interpolation scheme is commonly used to transfer the precise boundary conditions at the surrounding computational points [21,22]. However, in clinical applications, the position of the LV boundaries is extracted by semi-visual assessments from images whose resolution is lower than the computational grid; therefore, the uncertainty regarding the boundary position is commonly larger than the grid-size. Anatomically, the LV endocardium presents small-scale elements that are not resolved in imaging and are not reproduced in the extracted geometry. Finally, living geometries present continuous physiological variations and any instantaneous measurement must be considered within a range of its natural variability. Thus, in the context of simulations based on images and finalized to clinical applications, the time-consuming interpolation scheme can be cut down by simply closing all the faces of the cell containing the immersed boundary and setting a velocity equal to the average of the points falling in that cell. A computational step that can be performed with extreme efficiency. Additionally, when computing the Navier-Stokes equation at the closed cells corresponding to soft tissue, the cell viscosity is artificially increased to its maximum stable value

$$\nu_{IB} = \frac{1}{2\Delta t} \left(\frac{1}{\Delta x^2} + \frac{1}{\Delta y^2} + \frac{1}{\Delta z^2} \right)^{-1}. \quad (5)$$

This simplification avoids unrealistic sharp-edge boundaries, and improves the numerical convergence by preventing from the creation of small scales of sub-grid size. Physically, the spatial accuracy is still well above the uncertainties and the variability of the boundaries that are somehow “blurred” about the closed cells. It must be underlined that the enhanced viscosity (5) is applied only to those computational cells that contain the solid immersed elements and has the only function of spreading the influence of them to the entire cell. Its numerical value increases with decreasing computational time-step, Δt , stating that the influence of the solid is spread to the entire cell instantaneously in theory, which is translated in the numerical simulation to using the highest possible diffusion coefficient. The influence of using the approximation (5) for a hypothetically smooth boundary is analyzed in §3.2 below.

2.3. Valve dynamics

The LV geometry obtained from imaging expands and contracts during the cardiac cycle and represents the driving force for blood motion. Differently, the dynamics of the mitral valve leaflets is driven by the interaction with flow. We consider here a simplified model of interaction between flow and MV that does not involve detailed tissue material properties. The valve is assumed as a membrane that opens with the flow with few degrees of freedom under the constraint of maintaining the shape consistent with that extracted from images as described in §2.1. In general, the valve geometry is described by its coordinates $\mathbf{X}_v(\vartheta, s, \varphi_i)$ where the parameters $\varphi_i(t)$, with $i = 1, 2 \dots N$, represent the N degrees of freedom modulating valvular dynamics. The valve geometry is thus known once the value of each parameter is known.

The statement that the valve opens with the flow translates mathematically in the congruence condition that the normal component of the valve velocity matches that of the fluid

$$\mathbf{v} \cdot \mathbf{n} = \sum_{i=1}^N \left(\frac{\partial \mathbf{X}_v}{\partial \varphi_i} \cdot \mathbf{n} \right) \frac{\partial \varphi_i}{\partial t}; \quad (6)$$

where \mathbf{n} is the local normal to the valvular surface. Equation (6) applies in general at every point of the continuous valvular surface. In [9], equation (6) was transformed in a single global equation by integration over the entire MV surface A_v that could be satisfied only in the case of a single degree of freedom ($N = 1$).

In general, the valve contains a finite number N of degrees of freedom and its overall dynamics is described by the combination of the individual terms $\frac{\partial \varphi_i}{\partial t}$. In this case, a solution in weak form of (6) can be obtained by minimization of its square root error integrated over the valvular surface

$$\iint_{A_v} \left\{ \mathbf{v} \cdot \mathbf{n} - \sum_{i=1}^N \left(\frac{\partial \mathbf{X}_v}{\partial \varphi_i} \cdot \mathbf{n} \right) \frac{\partial \varphi_i}{\partial t} \right\}^2 dA = \min. \quad (7)$$

The least square minimization is recast in the form of a linear system

$$\sum_{j=1}^N \left[\iint_{A_v} \left(\frac{\partial \mathbf{X}_v}{\partial \varphi_i} \cdot \mathbf{n} \right) \left(\frac{\partial \mathbf{X}_v}{\partial \varphi_j} \cdot \mathbf{n} \right) dA \right] \frac{\partial \varphi_j}{\partial t} = \iint_{A_v} (\mathbf{v} \cdot \mathbf{n}) \left(\frac{\partial \mathbf{X}_v}{\partial \varphi_i} \cdot \mathbf{n} \right) dA, \quad (8)$$

on the N unknowns $\frac{\partial \varphi_i}{\partial t}$, $i = 1, 2, \dots, N$, that specify the motion of the valve due to the blood flow starting from the initial closed configuration $\varphi_i(0) = 0$. The matrix of the system (8)

$$M_{ij} = \iint_{A_v} \left(\frac{\partial \mathbf{X}_v}{\partial \varphi_i} \cdot \mathbf{n} \right) \left(\frac{\partial \mathbf{X}_v}{\partial \varphi_j} \cdot \mathbf{n} \right) dA, \quad (9)$$

represents the mutual influence of the different degrees of freedom, it is a diagonally-dominant and symmetric matrix and ensures that the system is well conditioned.

The model (8) was introduced here with reference to the specific application for cardiac valves. Nevertheless, the mathematical framework is rather general and not bounded to this application. It works with an arbitrary geometry, here called \mathbf{X}_v , whose possible configurations are described by a finite number of degrees of freedom each one quantified by the corresponding parameter, that in this case are the φ_i 's. These degrees of freedom may represent spatially distinct elements, as it is in this case, or they could represent parameters of a spectral representation or even mixed descriptions.

In the limit of $N \rightarrow \infty$ this model represents a totally loose surface where all points moves as if they were independent particles. When N is small, this approach to valve dynamics represents a modal decomposition where the overall motion is simplified in a few modes (degrees of freedom). It must be emphasized that the model (8) represents a drastic simplification with respect to a complete FSI approach because the equations governing the deformation of the tissue are not explicitly included. Thus this model neglects the forces due to elastic recall and reproduces the asymptotic behavior where the valve moves with the flow with no elastic resistance other than the constraint of ensuring that the MV geometry agrees with that obtained from the clinical images. The approximation of this model with respect to a FSI is paid back by the advantage of allowing simulations solving a simple linear system and without requiring a detailed definition of tissue properties that cannot be measured in vivo.

The dynamics described by the system (8) represents the asymptotic limit of the loosest MV within the prescribed set of geometric configurations. As such, it also provides a reference ground for the introduction of additional factors accounting for elastic resistance based on clinical observables. For example, in a MV model it is natural to consider a description with two degrees of freedom corresponding to the motion of the two leaflets. In this case, the leaflets' stiffness affects the timing of opening or closure, which can be measured relatively easily in vivo using ultrasound echo M-mode imaging. The effect of elastic stiffness can be added over the asymptotic model, like it was done in [4] in a former model with one degree of freedom. In analogy to that approach, for example, the stiffness corresponding to each individual degree of freedom can be added to the corresponding equation of the system (8) using a term that depends on the deformation associated to that degree of freedom. Each additional term introduces additional coefficients that should then be calibrated with the measurements of the corresponding phenomena.

The system (8), that gives $\frac{\partial \varphi_i}{\partial t}$, is evaluated in parallel to the Navier-Stokes equation (2), that gives $\frac{\partial \mathbf{v}}{\partial t}$, during the substeps of the Runge-Kutta time advancement of fluid velocity and valve position. At the completion of the time step, the fluid boundary conditions are imposed at all immersed boundaries including the valve position based on the instantaneously computed valve motion, and the Poisson equation (4) is solved accordingly, this feedback completes the interaction between tissue and blood flow.

Finally, the aortic valve, which is downstream of the LV flow field, is modeled as a simple orifice with a flat surface that is either open or closed. Aorta is considered open when the mitral valve is closed and the normal velocity, averaged over the position of the aortic valve surface, prior to setting the boundary conditions, is directed outwards. This way, it is not necessary to prescribe the open or closed state of the aortic valve by global considerations because the exact instants of start-end of systole and diastole can be difficult to define accurately in pathological conditions.

3. Verifications

3.1. Numerical verification

The overall numerical implementation was extensively validated in previous studies. However, simulations of coupled problems involving both fluid and solid elements are often challenging and results can be dependent on space and time resolution even when the convective and diffusive stability criteria are fulfilled. Therefore, we preliminarily performed an extensive validation of the numerical method to verify the sensitivity of results to specific numerical choices. To this aim we considered a single degree of freedom valve model and a simple LV geometry used in a previous study [9]. We show here the results for a same system simulated with a basic grid made of $128 \times 128 \times 160$ points and 2048 time steps in one heartbeat, a refined grid $192 \times 192 \times 240$ points and 3072 time steps, and the same eliminating the model for atrium and aorta thus allowing inflow/outflow to communicate in the space surrounding the LV. The coarser parameters were previously demonstrated to ensure convergence of flow solution with valves modeled as orifices without moving leaflets [10,19,20]. We monitored here the MV opening angle, that represents the result of the interaction between flow and solid elements, for which minor instantaneous differences can trigger progressively increasing discrepancies.

The results of leaflet dynamics, reported in Fig. 3, are very similar within this range of spatial and temporal resolution and are not influenced by the presence of atrium/aorta models, which only reduces phenomena of vortex interaction outside the LV. These results demonstrate the robustness of the coupled computational model, possibly because it is based on integral balances. The flow fields are essentially identical in the three cases.

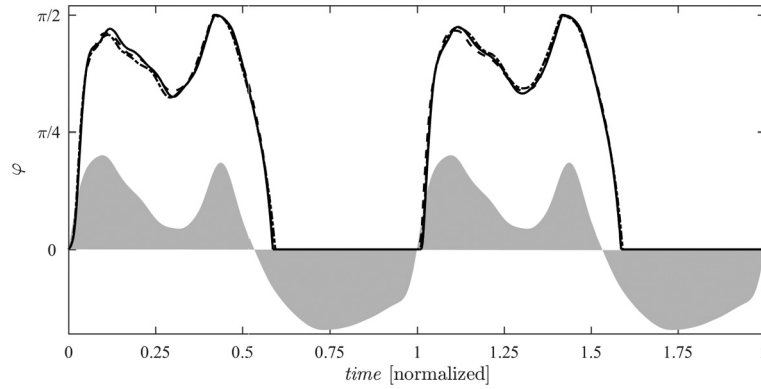


Fig. 3. Time course of the valve opening angle in three cases with different resolution and removing the model of atrium and aorta upstream and downstream of the valvular plane, respectively. The continuous line represents basic grid made of $128 \times 128 \times 160$ points; the dashed line represents a refined grid $192 \times 192 \times 240$ points; and the dashed point line represents the same, only eliminating the model for atrium and aorta. The shaded gray area represents the volume rate for reference (not to scale).

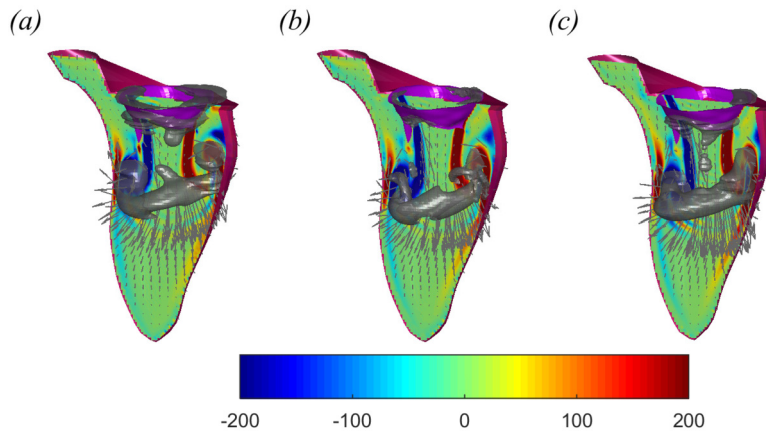


Fig. 4. Flow fields in a normal LV at peak E-wave computed (a) with regular viscosity, (b) with the enhanced viscosity at the immersed boundary using identical numerical parameters, and (c) with the enhanced viscosity and half time step. Each picture shows the color-map of the normal vorticity (red to blue from -200 to 200 , units equal to the inverse of the heartbeat period) and the velocity vectors (every 4 grid points) on a longitudinal plane crossing the center of MV, of aorta and LV apex; the three-dimensional gray surfaces represents iso-surfaces of the λ_2 parameter.

3.2. Effect of immersed boundary viscosity

The IBM method for flow simulation presented in §2.2 proposes to use an amplification of the viscosity coefficient, equation (5) when the fluid equations are evaluated in correspondence of the immersed solid elements. The appropriateness of such a method was suggested when the uncertainty in the boundary position is larger than the grid size because the method spreads the boundary condition over the computational cell.

We perform here a comparative analysis between numerical solutions obtained with and without the introduction of equation (5) to verify the influence of this assumption with respect to considering a smooth boundary. We also performed the same simulation halving the time step to verify the potential influence of time step on equation (5). The comparison is carried out in the case of a normal LV (details about this case are described below in §4). Results show that the flow is largely unaffected by the introduction of this artificial boundary viscosity, with the only difference limited to the presence of very small scales that are sometime smoothed out in presence of the enhanced viscosity. As an example, Fig. 4 shows the flow fields at the peak of the E-wave in the three cases.

The comparative analysis provides some support that this approach does not introduce non-physical phenomena other than smearing out grid-size fluctuations near the boundaries, a phenomenon that is meaningful when the position of the boundary is not known with accuracy.

In particular, it can be useful in presence of sharp boundaries that are a result of segmentation algorithms and whose details may not be physically realistic. In such case, the immersed boundary approach can give rise to similarly unrealistic small scales in fluid flow. To better describe this point, Fig. 5 shows three insets with the enlargement of the vorticity field near sharp boundaries computed with and without artificial viscosity at the solid cells. The zero-thickness boundaries sometime produces fluctuations of length equal to the grid size that are a consequence of the jump across the solid cell. Such fluctuations are significantly reduced when the viscosity is enhanced at boundary cells.

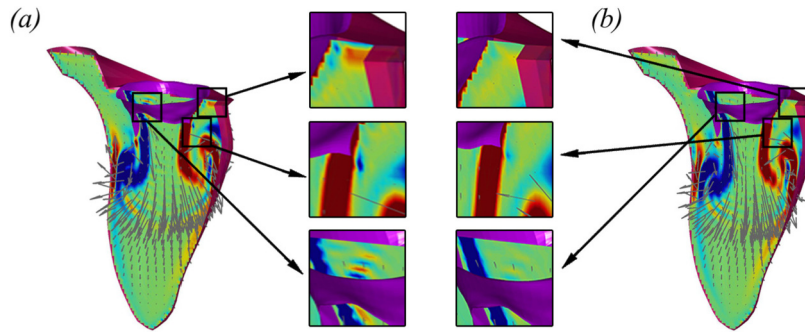


Fig. 5. Details of the flow fields in a normal LV at peak E-wave computed (a) with regular viscosity, (b) with the enhanced viscosity at the immersed boundary using identical numerical parameters. Each picture shows the color-map of the normal vorticity (red to blue from -200 to 200 , units equal to the inverse of the heartbeat period) and the velocity vectors (every 4 grid points) on a longitudinal plane crossing the center of MV, of aorta and LV apex. The three panels report enlarged views of specific regions next to edges of the immersed boundary.

It must also be reminded that this artificial viscosity is applied only to those computational cells that contain the solid elements. Such cells are treated as fluid cells during the IBM solution and the flow equation are solved therein during the intermediate time-advancement steps when discontinuities can influence nearby fluid cells. The enhanced viscosity essentially reduces this influence and has the main effect of spreading the presence of the solid to the entire cell. At the same time, this approach can improve the stability of the numerical solution in presence of sharp boundaries; therefore, it may reduce the need of smoothing procedures when preprocessing the borders obtained from image segmentation tools.

Therefore, the usage of equation (5) appears appropriate when the definition of the anatomical boundaries is available with a resolution that is comparable to the grid size or when such boundaries are described with unphysical sharp edges.

3.3. Comparison with a FSI solution

The computational model is preliminarily evaluated in an idealized geometry where a FSI solution is available from a study in literature for a healthy LV with a simplified natural MV made of two separate leaflets [21]. The LV presents a volumetric reduction of 60% with respect to its maximum size. This corresponds to a peak Reynolds number $Re = \frac{v_p D_a}{\nu} \simeq 4200$, where v_p is the maximum velocity averaged across the mitral annulus of diameter D_a , and a Strouhal number $St = \frac{D_a}{v_p T} \simeq 2.9 \times 10^{-2}$ and T is the heartbeat duration. It is worthwhile to remark that the peak velocity lasts only for a small fraction of the cycle and the average value of the Reynolds number is about 660 and of Strouhal 0.18. The MV tissue properties are assumed in the FSI solution as those of an isotropic linearly-elastic membrane of uniform (small) thickness, which includes mass and bending stiffness [7,21]. For the present comparison, mimicking the procedure proposed for application to clinical data, the LV geometry coming from the FSI numerical solutions and the MV geometry in the open and closed configurations are used as input for the present model. The MV geometry is here described by 2 degrees of freedom that exactly identify the individual leaflets.

It is important to remark that the two systems are not directly comparable. The FSI simulation is obtained with a specific set of values for the valvular tissue properties, whereas such properties are not part of the present asymptotic model where the leaflets motion is not subjected to elastic resistance. Moreover, the valve in FSI has a small mass while the equation of motion (8) in the present model does not include a term accounting for the inertia of the MV. However, this difference is minor as the valvular tissues occupy a small volume, their density is comparable to that of surrounding blood whose inertia is implicitly accounted in the Navier–Stokes equations. Therefore, this comparative analysis is not aimed to a one-to-one comparison given the differences between the physical systems; it rather allows to verify the consistency of the asymptotic model considering that the main difference is the absence of bending stiffness.

Computations are performed starting from rest in both models and are limited to the first diastole. Fig. 6a–c shows the velocity fields obtained by the FSI solution corresponding to three time instants (peak of the E-wave, stasis between E and A waves, and peak of A-wave), and are compared with those obtained at the same instants with the present model (Fig. 6d–f). Both models show similar gross features, with the entering jet displaced towards the lateral wall (on the right side) in Fig. 6a,d, a weak downward flow pattern about the valve leaflets in Fig. 6b,e, and a straight jet in Fig. 6c,f. The two numerical results differ mainly for the apparent different degree of smoothness. This is partly imputable to the different numerical techniques; moreover, in order to create the same graphical representation, the present results were resampled from the staggered grid with (2x2 filtering) and the flow field inside was cropped.

Some differences are also a consequence of differences in the valvular dynamics. A first comparison of the motion of the anterior leaflet in the two cases is reported in Fig. 7, using the same representation of the original FSI reference [21]; the motion of the posterior leaflet, not reported here, shows analogous behavior although with excursions that are about 20 times smaller. The curves suggest that the present model corresponds to a system with looser leaflets: the leaflet opens more rapidly during the E-wave, it presents a slightly larger closure during diastasis, and opens completely during the E-wave when the elastic leaflets of the FSI model do not reach complete opening.

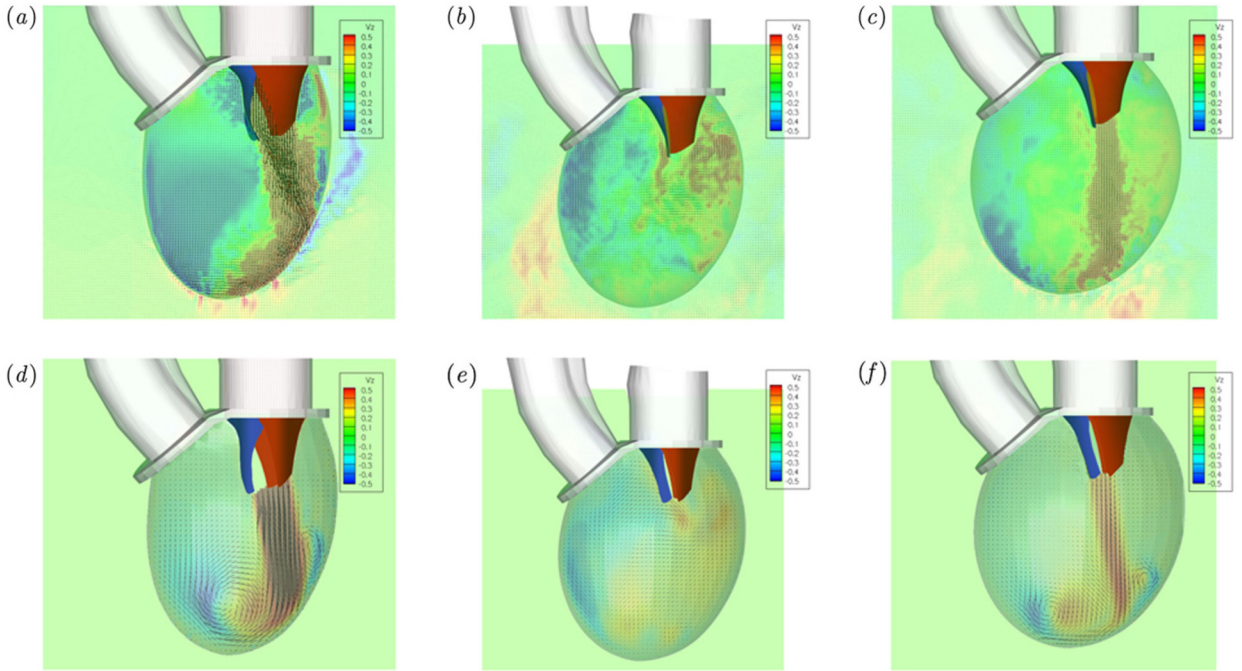


Fig. 6. Snapshots of the velocity field in the central transversal plane, $y = 0$, for the idealized system introduced in [21]. Results from the FSI numerical study (a,b,c) and from the present model (d,e,f). The flow fields corresponds to peak E-wave (a,d), diastasis (b,e), peak A-wave (c,f); each picture reports the velocity vectors and the colormap of the vertical velocity. (Due to different graphical representations, the color pattern in (d,e,f) results smoother and cropped inside the valve.)

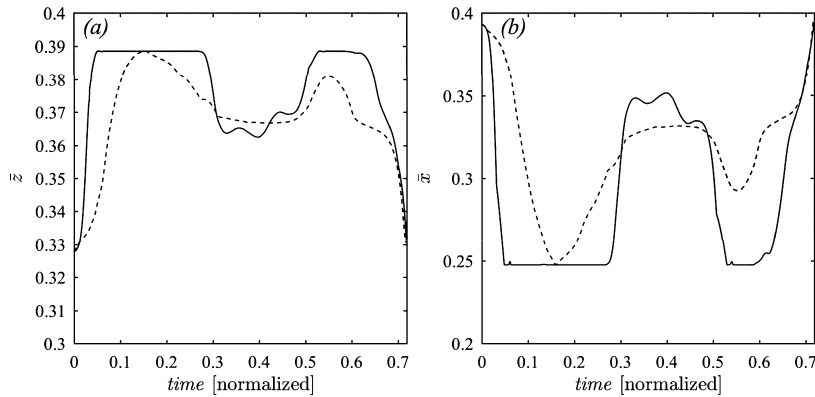


Fig. 7. Time evolution of the mean z -coordinate (a), and of the mean x -coordinate (b) for the anterior leaflet: continuous line for the present asymptotic model, dashed line for the elastic FSI model.

Another quantitative comparisons is reported in Fig. 8 in terms of metrics more directly related to valvular function like the projected opening area $A(t)$, and the average cross-valve velocity $v(t)$ (computed as Q_e/A , where Q_e is the effective volume rate across the valvular opening, as defined later in equation (10)). The comparison between the opening areas in Fig. 8(a) confirms that the present model corresponds to a looser valve that responds more rapidly both during opening and closure. This difference does not affect significantly the value of fluid velocity, shown in Fig. 8(b); this is also due to the specific geometry of the leaflets for this valve, visible in Fig. 6, that are extended in length with a large lateral opening and a motion that is mainly transversal. The quicker opening in the asymptotic model gives rise to a lower velocity during acceleration and a peak flow that is reduced of about 6%, in this case, but that may become more significant in other situations.

In summary, considering the existing difference between the two systems, it was not expected that the asymptotic model results match very closely to the FSI results. The comparative analysis shows that the present model corresponds to MV dynamics where the leaflets movements are more rapid with respect to having elastic resistance with an overall congruence of the coupled MV-LV fluid dynamics. These results provide a further partial support that the model is compatible with the assumption of asymptotic behavior.

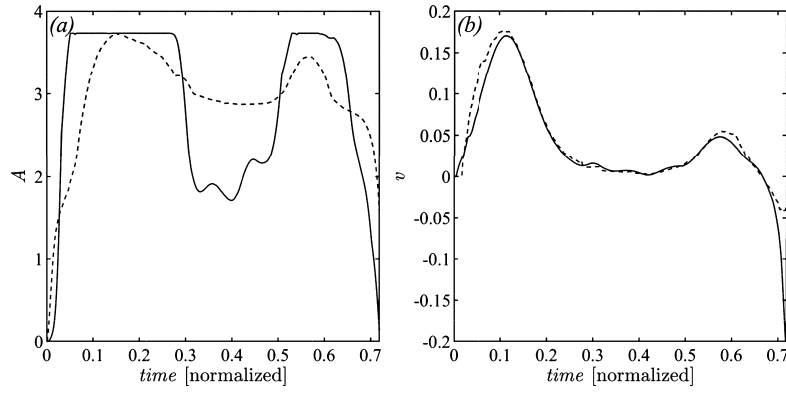


Fig. 8. Time evolution of the projected valve opening area (a), and of the mean cross-valve vertical velocity (b): continuous line for the present asymptotic model, dashed line for the elastic FSI model.

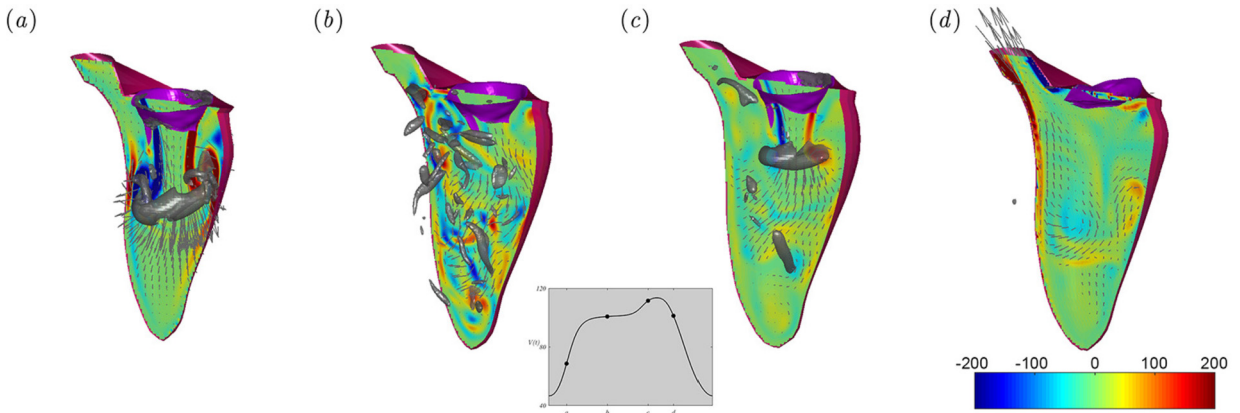


Fig. 9. Flow fields in the normal LV, computed with the two degrees of freedom model, at four instants: (a) peak E-wave, (b) diastasis, (c) A-wave, (d) early systole; as indicated in the volume curve inset. Each picture shows the color-map of the normal vorticity (red to blue from -200 to 200 units equal to the inverse of the heartbeat period) and the velocity vectors (every 4 grid points) on a longitudinal plane crossing the center of MV, of aorta and LV apex; the three-dimensional gray surfaces represents one iso-surface of the λ_2 parameter.

4. Application to a normal LV

4.1. Fluid dynamics

The computational model is here applied to a normal healthy LV extracted from images as described in §2.1. The cardiac function is characterized by an end-diastolic volume $EDV = 113$ ml, end-systolic volume $ESV = 47$ ml, stroke volume $SV = EDV - ESV = 67$ ml, and ejection fraction $EF = \frac{SV}{EDV} = 59\%$. The specific volumetric curve, gives a velocity at peak diastole of approximately $v_p \simeq 46$ cm/s averaged across the annulus area (whose diameter is approximately $D_a \simeq 3.3$ cm). These figures correspond to a peak Reynolds number $Re = \frac{v_p D_a}{\nu} \simeq 3800$ and a Strouhal number $St = \frac{D_a}{v_p T} \simeq 7.2 \times 10^{-2}$. However, the effective peak Re reaches about 1.7 times this value because the effective orifice area of the open mitral valve is smaller than the annulus; although such high values are found for a very limited period of time and the average Re during the entire diastole is about 940.

The flow field is shown in Fig. 9 at four instants during the cardiac cycle. The overall intraventricular fluid dynamics is qualitatively analogous to that previously described in literature with either orifice-like or different models of the mitral valve in various different geometries of normal LVs [28,23,37,12]. During the early-filling an asymmetric vortex jet, whose head is a deformed vortex ring, enters the LV. The vortex structure interacts with the boundary layer of the lateral wall (right in the pictures) and partly dissipates in diastasis leaving a weak clockwise circulation occupying most of LV, while a second vortex ring follows during the atrial filling. It is worth to note that this second ring is more regular because it is released by the rapid closure of the MV mouth at the onset of systole, when a weak circulation drives the flow toward the outflow tract.

The corresponding time course of the two leaflets opening angle is reported in Fig. 10. The leaflets show a rapid opening during the acceleration phase of the E-wave reaching the complete opening before the maximum flow, which is in agreement with clinical observation. A small partial closure occurs during the diastasis period, between the E and A waves. At

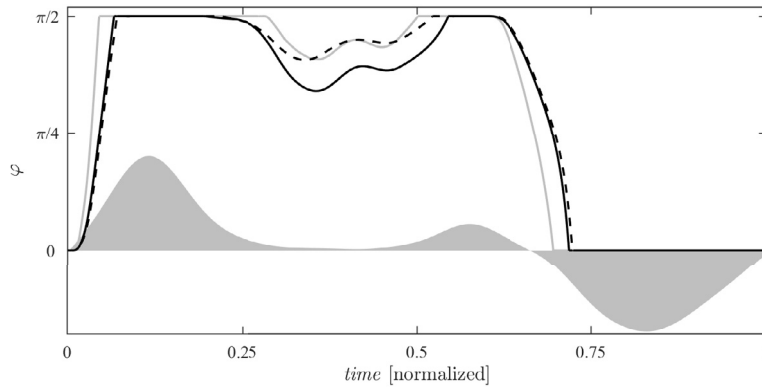


Fig. 10. Time course of the mitral valve opening angles in a normal LV. Continuous lines are the anterior (black) and posterior (gray) leaflets opening angles in the 2 degrees of freedom model; the dashed line is the result for a single degree of freedom model. The shaded gray represents the volume rate for reference (not to scale).

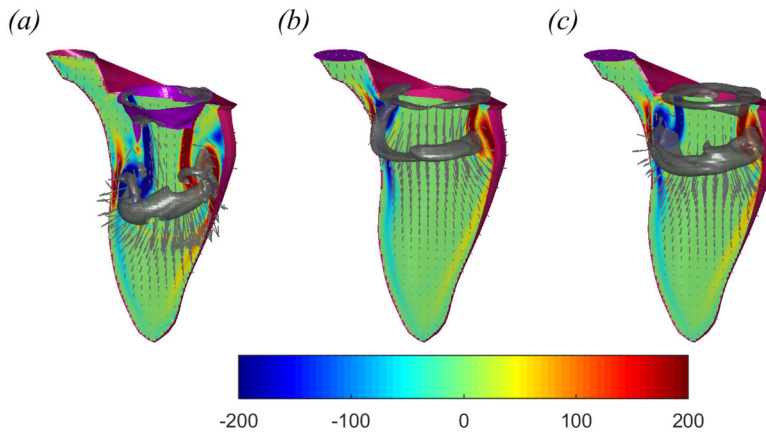


Fig. 11. Flow fields in the normal LV at the peak of E-wave, (a) computed with the two degrees of freedom mitral valve model, (b) with a valveless circular orifice in mitral position at the annulus, (c) with a valveless circular orifice of the same area of the open mitral valve. Each picture shows the color-map of the normal vorticity (red to blue from -200 to 200 units equal to the inverse of the heartbeat period) and the velocity vectors (every 4 grid points) on a longitudinal plane crossing the center of MV, of aorta and LV apex; the three-dimensional gray surfaces represents one iso-surface of the λ_2 parameter.

the end of diastole, closure starts at the deceleration phase of the A-wave, due to the adverse pressure gradient, and quickly completes during the acceleration of the systolic wave. The shorter, posterior leaflet is quicker in the early opening and the final closure while the longer anterior leaflet follows shortly after it. As a further check, the same picture reports the opening angle computed by the MV model with one degree of freedom, which presents a comparable valvular movement.

4.2. Comparison with valveless mitral orifice

The intraventricular flow that develops in a normal LV in presence of the MV is here compared with the flow obtained when the valve is replaced by a circular orifice without leaflets, which is open in diastole and closed in systole (so-called *diode* model). In the comparison we first consider an orifice at the position of the annulus, whose effective area is larger than that of the actual MV, then we consider an orifice with an area that is equal to the MV area in the open configuration.

The flow fields are shown in Fig. 11 at the peak of the E-wave, one instant that is directly influenced by the MV opening phase. The vortex ring that develops from the larger orifice (Fig. 11b) is more regular, wider and remains closer to the base with respect to that found with the MV model (Fig. 11a). This result was expected because the circular orifice has a regular trailing edge and the velocity of the fluid crossing the mitral orifice is smaller.

Interestingly, a similar result with a regular and basal vortex ring is also found when the valveless orifice has the same size of the open MV (Fig. 11c). Although the ring is stronger than before, it remains fairly regular being shed from a planar circular orifice, moreover it remains closer to the base despite the transvalvular fluid velocity is comparable to that in the MV model. This is first imputable to the fact that the boundary layer separation occurs from the LV base instead of the MV leaflets trailing edge that lay downstream. Moreover, the ring is stretched and enlarged by the background (initially irrotational) flow associated to the fixed orifice that expands rapidly behind a circular sharp edge facing the flow. This

behavior is very different in presence of an opening valve that drives the flow in a funnel-like stream with velocities that are initially higher and are directed downstream after the trailing edge.

4.3. Interpretation of MV dynamics

Physically, valvular opening is driven by the incoming transmitral flow when the LV pressure falls below the pressure in the left atrium and pressure difference is large enough for accelerating the entire fluid volume corresponding to the filling flow rate $\frac{dV}{dt}$. Valvular opening can thus be described with the aid of conservation of mass [27].

Consider a control volume bounded by the surface within the mitral annulus, the instantaneous valvular surface, and the orifice area inside the trailing edge, $\mathbf{X}_e = \mathbf{X}_v(\vartheta, 1)$, the expression of mass balance states that the total volume rate crossing the annulus is balanced by the volume allowed by the displaced valve surface plus the flow Q_e across the trailing edge orifice

$$\frac{dV}{dt} = \iint_{A_v} \mathbf{v} \cdot \mathbf{n} dA + Q_e. \quad (10)$$

When elastic resistance can be neglected, it can be hypothesized that the valve opens with the flow without developing significant vortex shedding from the trailing edge [26]. This means that an estimation of the velocity across the orifice does not differ significantly from that of the trailing edge $\frac{\partial \mathbf{X}_e}{\partial t}$. Within this assumption, the discharge Q_e can be estimated by integrating along a line, L , separating the anterior and posterior trailing edges, taking the area between the facing edges and using the component normal to such area of the mean velocity between them

$$Q_e \cong \int_L \frac{1}{2} \left(\frac{\partial \mathbf{X}_{e_{post}}}{\partial t} + \frac{\partial \mathbf{X}_{e_{ant}}}{\partial t} \right) \cdot \mathbf{n} |\mathbf{X}_{e_{post}} - \mathbf{X}_{e_{ant}}| dL. \quad (11)$$

Equations (10), with Q_e given by 11, provides a relationship between the LV volumetric variation and valvular motion under the assumption of negligible vortex shedding.

This relationship can be made more explicit when valve motion is described by a single degree of freedom, $\varphi(t)$. Using (6) with $N = 1$ to rewrite the time derivatives, equation (10) can be rewritten

$$\frac{dV}{dt} = \left[\iint_{A_v} \frac{\partial \mathbf{X}}{\partial \varphi} \cdot \mathbf{n} dA + \hat{Q}_e \right] \frac{\partial \varphi}{\partial t}; \quad (12)$$

where

$$\hat{Q}_e \cong \int_L \frac{1}{2} \left(\frac{\partial \mathbf{X}_{e_{post}}}{\partial \varphi} + \frac{\partial \mathbf{X}_{e_{ant}}}{\partial \varphi} \right) \cdot \mathbf{n} |\mathbf{X}_{e_{post}} - \mathbf{X}_{e_{ant}}| dL. \quad (13)$$

For a given flow rate $\frac{dV}{dt}$, equation (12) represents a first order ordinary differential equation for the opening angle $\varphi(t)$. It can be integrated with initial condition $\varphi(0) = 0$, to provide an estimate of the initial phase of valvular opening.

The valvular motion obtained by (12) is shown in Fig. 12 and compared with that obtained from the numerical results. The overall agreement is satisfactory for short times, the difference increases as the valve approaches its maximum opening when some shedding develops and the formula (11), or (13), becomes increasingly approximated. This result supports the interpretation that the asymptotic model in §2.3 corresponds to a valvular opening driven by the fluid crossing the MV without resistance, such that the loose trailing edge moves in close accordance to the fluid velocity and vortex shedding is initially negligible. In this case, valvular opening is essentially a kinematic effect following mass conservation and it does not depend on the geometric properties of the LV other than the flow rate.

Analogous arguments can be applied to the description of the valvular closure at the transition between diastole and systole. Physically, MV closure starts for the large adverse pressure gradient associated with the deceleration of the late diastolic transmitral flow and continues rapidly during the acceleration of the backward directed systolic wave with no significant role played by the vortices in the LV [18,35]. Indeed, the vortex-induced velocities are low (few cm/s) and the associated pressure are negligible with respect to the intracardiac pressure differences at the onset of systole. In agreement with the normal physiology, result show that MV closure completes during the beginning of systole. This effect is associated to the phenomenon of false back flow when the blood contained inside the MV cup returns into the atrium when leaflets close. During this phase, a possible elastic recall may facilitate valvular closure although this effect is expected to be small.

Differently, the ventricular vorticity might contribute to the partial valve closure during the diastasis when transvalvular flow rate is small or absent [35]. In this phase of the cardiac cycle, the vortex-induced rotational velocity pattern inside the LV may create a weak overpressure over the downstream face of the leaflets (especially the longer anterior leaflet) and support partial closure. This phenomenon, which is found in the present result, is very variable in clinical observations where closure in diastasis ranges from being negligible to complete.

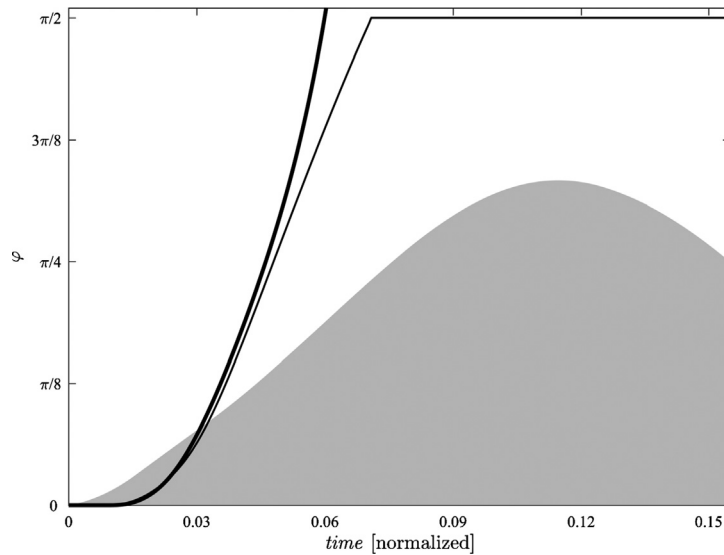


Fig. 12. Valvular opening at the onset of diastole as computed by the numerical simulation (thin line) and estimated from the approximation for short times assuming valve with no resistance (thick line). The shaded gray represents the volume rate for reference (not to scale).

5. Discussion of model limitations

The computational model introduced here should not be confused with a FSI model, primarily because it does include the elastic properties of the tissues that would be required to solve the momentum equation for the solid elements. Therefore, it describes an asymptotic behavior only and was designed to provide a relatively straightforward application of LV flow simulations in clinical conditions when the mechanical properties of tissue are not available or cannot be extrapolated. To reach this objective, the model includes a number of simplifications that correspond to a series of limitations that are briefly summarized here.

First of all, the set of possible valve configurations is given a-priori as a function of few evolutionary parameters (degrees of freedom). Hence, there is no guarantee that the effective deformation of the tissue elements belongs to such a pre-defined set of configurations; the actual reliability depends on the reliability and completeness of the information used to create such configurations and to the associated degrees of freedom. Secondly, the fluid-tissue interaction describing MV motion represents an asymptotic behavior where the valve moves with the flow with no resistance given by an internal anatomic structure other than the constraint of moving inside the set of predefined configurations. Therefore, the model corresponds to the loosest tissue dynamics within those geometric configurations. In perspective, however, the system (8) may be integrated with additional terms representing elastic resistance. These terms will depend on the deformation associated to the relative degree of freedom, like in [4], and include coefficients that should be calibrated to additional measurements. Finally, the model also neglects the influence of chordae tendineae that ensure unidirectional flow by constraining the valve from opening toward the atrium. In this regard, this study did not consider additional effects imputable to the chordae, such as their tethering that may influence MV dynamics in dilated LVs. It also neglects the possible impact of leaflets with surrounding tissues, that are simply anticipated by limiting the allowed configurations.

As discussed in the introduction, a complete FSI approach is the only methodology for ensuring complete reproduction of the dynamics for both fluid and solid phases [13,21,15,16,12,40,3]. On the other hand, the development of FSI in living biological systems presents exceptional difficulties in the definition of tissue properties, including constitutive equation and elastic parameters which may be space-varying and non-isotropic [34,5,17], that cannot be easily estimated in vivo. In general, in the perspective of a clinical application, we are left with a dichotomy between simplified approximated models, that may agree with limited measurable information but may not be generally valid, and complete FSI models based on an approximation of the effective set of tissue parameters that may not be realistic for the specific case under analysis. Aware of these limited options, the present model follows the first route introducing a clinical imaging-based approach, with the objective of providing one additional possible approach.

The present model -within the limitations described above- describes an asymptotic behavior that may provide some bounds to the many possible results; it also provides a possible reference for improvements able to include further phenomena.

6. Conclusions

This study presented a numerical approach to the LV fluid dynamics that includes the interaction with MV leaflets. The method is designed for integration with medical imaging in compliance with the accuracy of information effectively

available in clinical applications. This model of valvular dynamics corresponds to an asymptotic description of leaflet motion when information about tissue properties are not available or cannot be extrapolated.

It represents an improvement with respect to using valveless orifice and provides a more realistic reproduction of the flow below the valve. This over-simplified approach to the interaction between flow and solid elements could be extended to different applications and integrated with parametric description of global tissue properties.

Declaration of competing interest

The authors declare that they have no known competing financial interests or personal relationships that could have appeared to influence the work reported in this paper.

References

- [1] L. Andres-Delgado, N. Mercader, Interplay between cardiac function and heart development, *Biochim. Biophys. Acta, Mol. Cell Res.* 1863 (2016) 1707–1716.
- [2] B. Baccani, F. Domenichini, G. Pedrizzetti, Model and influence of mitral valve opening during the left ventricular filling, *J. Biomech.* 36 (2003) 355–361.
- [3] L. Boilevin-Kayl, M.A. Fernández, J.F. Gerbeau, Numerical methods for immersed FSI with thin-walled structures, *Comput. Fluids* (2018), <https://doi.org/10.1016/j.compfluid.2018.05.024>.
- [4] C. Celotto, L. Zovatto, D. Collia, G. Pedrizzetti, Influence of mitral valve elasticity on flow development in the left ventricle, *Eur. J. Mech. B, Fluids* 75 (2019) 110–118.
- [5] L. Chen, F.C. Yin, K. May-Newman, The structure and mechanical properties of the mitral valve leaflet-strut chordae transition zone, *J. Biomech. Eng.* 126 (2004) 244–251.
- [6] J.C. Culver, M.E. Dickinson, The effects of hemodynamic force on embryonic development, *Microcirculation* 17 (2010) 164–178.
- [7] M.D. de Tullio, G. Pascazio, A moving least-squares immersed boundary method for simulating fluid-structure interaction of elastic bodies with arbitrary thickness, *J. Comput. Phys.* 235 (2016) 201–225.
- [8] F. Domenichini, On the consistency of the direct forcing method in the fractional step solution of the Navier-Stokes equations, *J. Comput. Phys.* 227 (2008) 6372–6384.
- [9] F. Domenichini, G. Pedrizzetti, Asymptotic model of fluid–tissue interaction for mitral valve dynamics, *Cardiovasc. Eng. Technol.* 6 (2015) 95–104.
- [10] F. Domenichini, G. Pedrizzetti, Hemodynamic forces in a model left ventricle, *Phys. Rev. Fluids* 1 (2016) 83201.
- [11] J. Eriksson, J. Zajac, U. Alehagen, A.F. Bolger, T. Ebbers, C.-J. Carlhall, Left ventricular hemodynamic forces as a marker of mechanical dyssynchrony in heart failure patients with left bundle branch block, *Sci. Rep.* 7 (2017) 2971.
- [12] H. Gao, L. Femnga, N. Qi, C. Berry, B.E. Griffith, X. Luo, A coupled mitral valve-left ventricle model with fluid-structure interaction, *Med. Eng. Phys.* 47 (2017) 128–130.
- [13] A. Gilmanov, T.B. Le, F. Sotiropoulos, A numerical approach for simulating fluid structure interaction of flexible thin shells undergoing arbitrarily large deformations in complex domains, *J. Comput. Phys.* 300 (2015) 814–843.
- [14] J.R. Hove, R.W. Köster, A.S. Forouhar, G. Acevedo-Bolton, S.E. Fraser, M. Gharib, Intracardiac fluid forces are an essential epigenetic factor for embryonic cardiogenesis, *Nature* 421 (2003) 172–177.
- [15] K.S. Kunzelman, D.R. Einstein, R.P. Cochran, Fluid-structure interaction models of the mitral valve: function in normal and pathological states, *Philos. Trans. R. Soc. B* 362 (2007) 1393–1406.
- [16] K.D. Lau, V. Diaz, P. Scambler, G. Burriesci, Mitral valve dynamics in structural and fluid-structure interaction models, *Med. Eng. Phys.* 32 (2010) 1057–1064.
- [17] C.H. Lee, R. Amini, S.C. Gorman, J.H. Gorman III, M.S. Sacks, An inverse modeling approach for stress estimation in mitral valve anterior leaflet valvuloplasty for in-vivo valvular biomaterial assessment, *J. Biomech.* 47 (2014) 2055–2063.
- [18] C.S.F. Lee, L. Talbot, A fluid-mechanical study of the closure of heart valves, *J. Fluid Mech.* 91 (1979) 41–63.
- [19] J.O. Mangual, F. Domenichini, G. Pedrizzetti, Three dimensional numerical assessment of the right ventricular flow using 4d echocardiography boundary data, *Eur. J. Mech. B, Fluids* 35 (2012) 25–30.
- [20] J.O. Mangual, E. Kraigher-Krainer, A. De Luca, L. Toncelli, A. Shah, S. Solomon, G. Galanti, F. Domenichini, G. Pedrizzetti, Comparative numerical study on left ventricular fluid dynamics after dilated cardiomyopathy, *J. Biomech.* 46 (2013) 1611–1617.
- [21] V. Meschini, M.D. De Tullio, G. Querzoli, R. Verzicco, Effects of natural and prosthetic mitral valves on the flow structure in healthy and pathological left ventricles, *J. Fluid Mech.* 834 (2018) 271–307.
- [22] R. Mittal, H. Dong, M. Bozkurtas, F.M. Najjar, A. Vargas, A. von Loebbecke, A versatile sharp interface immersed boundary method for incompressible flows with complex boundaries, *J. Comput. Phys.* 227 (2008) 4825–4852.
- [23] R. Mittal, J.H. Seo, V. Vedula, Y.J. Choi, H. Liu, H.H. Huang, S. Jain, L. Younes, T. Abraham, R.T. George, Computational modeling of cardiac hemodynamics: current status and future outlook, *J. Comput. Phys.* 305 (2016) 1065–1082.
- [24] D.R. Munoz, M. Markl, J.L.M. Mur, A. Barker, C. Fernández-Golfín, P. Lancellotti, J.L.Z. Gómez, Intracardiac flow visualization: current status and future directions, *Eur. Heart J. Cardiovasc. Imaging* 14 (2013) 1029–1038.
- [25] A. Pasipoularides, Mechanotransduction mechanisms for intraventricular diastolic vortex forces and myocardial deformations: part 2, *J. Cardiovasc. Transl. Res.* 8 (2015) 293–318.
- [26] G. Pedrizzetti, Kinematic characterization of valvular opening, *Phys. Rev. Lett.* 94 (2015) 1–4.
- [27] G. Pedrizzetti, F. Domenichini, Flow-driven opening of a valvular leaflet, *J. Fluid Mech.* 569 (2006) 321–330.
- [28] G. Pedrizzetti, F. Domenichini, Left ventricular fluid mechanics: the long way from theoretical models to clinical applications, *Ann. Biomed. Eng.* 43 (2015) 26–40.
- [29] G. Pedrizzetti, G. La Canna, O. Alfieri, G. Tonti, The vortex – an early predictor of cardiovascular outcome?, *Nat. Rev. Cardiol.* 11 (2014) 545–553.
- [30] G. Pedrizzetti, A.R. Martiniello, V. Bianchi, A. D'Onofrio, P. Caso, G. Tonti, Changes in electrical activation modify the orientation of left ventricular flow momentum: novel observations using echocardiographic particle image velocimetry, *Eur. Heart J. Cardiovasc. Imaging* 17 (2016) 203–209.
- [31] C.S. Peskin, Flow patterns around heart valves: a numerical method, *J. Comput. Phys.* 10 (1972) 252–271.
- [32] C.S. Peskin, The immersed boundary method, *Acta Numer.* 11 (2002) 479–517.
- [33] C.S. Peskin, D.M. McQueen, A three-dimensional computational method for blood flowing the heart I. Immersed elastic fibers in a viscous incompressible fluid, *J. Comput. Phys.* 81 (1989) 372–405.
- [34] T. Pham, W. Sun, Material properties of aged human mitral valve leaflets, *J. Biomed. Mater. Res., Part A* 102 (2014) 2692–2703.
- [35] H. Reul, N. Talukder, E.W. Mueller, Fluid mechanics of the natural mitral valve, *J. Biomech.* 14 (1981) 361–372.

- [36] P.P. Sengupta, G. Pedrizzetti, P.J. Kilner, A. Kheradvar, T. Ebbers, G. Tonti, A.G. Fraser, J. Narula, Emerging trends in cv flow visualization, *JACC Cardiovasc. Imaging* 5 (2012) 305–316.
- [37] J.H. Seo, V. Vedula, T. Abraham, A.C. Lardo, F. Dawoud, H. Luo, R. Mittal, Effect of the mitral valve on diastolic flow patterns effect of the mitral valve on diastolic flow patterns, *Phys. Fluids* 26 (2014) 121901.
- [38] V. Spandan, D. Lohse, M.D. De Tullio, R. Verzicco, A fast moving least squares approximation with adaptive Lagrangian mesh refinement for large scale immersed boundary simulations, *J. Comput. Phys.* 375 (2018) 228–239.
- [39] M. Vukicevic, D.S. Puperi, K.J. Grande-Allen, S.H. Little, 3d printed modeling of the mitral valve for catheter-based structural interventions, *Ann. Biomed. Eng.* 45 (2017) 508–519.
- [40] F. Xu, S. Morganti, R. Zakerzadeh, D. Kamensky, F. Auricchio, A. Reali, T. Hughes, M. Sacks, M. Hsu, A framework for designing patient-specific biopros-
thetic heart valves using immersogeometric fluid–structure interaction analysis, *Int. J. Numer. Methods Biomed. Eng.* 34 (2018) e2938.